



Article

Coupling Flank Collapse and Magma Dynamics on Stratovolcanoes: The Mt. Etna Example from InSAR and GNSS Observations

Giuseppe Pezzo ^{1,*} , Mimmo Palano ² , Lisa Beccaro ¹ , Cristiano Tolomei ¹ , Matteo Albano ¹ , Simone Atzori ¹ and Claudio Chiarabba ¹

¹ Istituto Nazionale di Geofisica e Vulcanologia, Osservatorio Nazionale Terremoti, 00143 Rome, Italy

² Istituto Nazionale di Geofisica e Vulcanologia, Sezione di Catania, Osservatorio Etneo, 95125 Catania, Italy

* Correspondence: giuseppe.pezzo@ingv.it

Abstract: Volcano ground deformation is a tricky puzzle in which different phenomena contribute to the surface displacements with different spatial–temporal patterns. We documented some high variable deformation patterns in response to the different volcanic and seismic activities occurring at Mt. Etna through the January 2015–March 2021 period by exploiting an extensive dataset of GNSS and InSAR observations. The most spectacular pattern is the superfast seaward motion of the eastern flank. We also observed that rare flank motion reversal indicates that the short-term contraction of the volcano occasionally overcomes the gravity-controlled sliding of the eastern flank. Conversely, fast dike intrusion led to the acceleration of the sliding flank, which could potentially evolve into sudden collapses, fault creep, and seismic release, increasing the hazard. A better comprehension of these interactions can be of relevance for addressing short-term scenarios, yielding a tentative forecasting of the quantity of magma accumulating within the plumbing system.

Keywords: Etna Volcano; SAR interferometry; advanced InSAR; GNSS; flank collapse; magma intrusion



Citation: Pezzo, G.; Palano, M.; Beccaro, L.; Tolomei, C.; Albano, M.; Atzori, S.; Chiarabba, C. Coupling Flank Collapse and Magma Dynamics on Stratovolcanoes: The Mt. Etna Example from InSAR and GNSS Observations. *Remote Sens.* **2023**, *15*, 847. <https://doi.org/10.3390/rs15030847>

Academic Editor: Eric Hetland

Received: 28 December 2022

Revised: 25 January 2023

Accepted: 31 January 2023

Published: 2 February 2023



Copyright: © 2023 by the authors. Licensee MDPI, Basel, Switzerland. This article is an open access article distributed under the terms and conditions of the Creative Commons Attribution (CC BY) license (<https://creativecommons.org/licenses/by/4.0/>).

1. Introduction

Surface deformation on active volcanoes represents the elastic/inelastic response to magma movements along the plumbing system, at depth. Deformations occur also in response to tectonic activity and/or gravitational flank instability [1], generally involving large sectors of a volcanic edifice, or lava cooling and soil subsidence, at very local scales. Deformations are commonly measured by using GNSS and InSAR techniques. The former technique provides a set of 3D geodetic observations at a limited number of points on the ground surface, allowing for collecting measurements at higher rates (up to 100 Hz). The latter technique provides a spatially dense set of geodetic measurements of ground deformation in the viewing geometry of the satellite sensor, and with a temporal sampling limited to the satellite orbital revisit (up to 6 days with the Sentinel constellations). Any deformation of the ground surface can be measured by comparing two SAR images of the same area, collected at different times from approximately the same position in space. InSAR processing advancements also allowed for multi-temporal analyses, which sensibly improved the investigation of long-term deformation patterns. GNSS and InSAR measurements can complement each other to infer the surface deformation over a target region.

An incredible variety of deformation patterns have been documented at Mt. Etna volcano (eastern Sicily, Italy; Figure 1) by geodetic datasets. Most of the studies have focused on specific deformation patterns related to distinct intrusive episodes [2–5] as well as on inflation/deflation events [6–10], providing useful information on the interaction between the plumbing system, local structures, and intrusive processes.

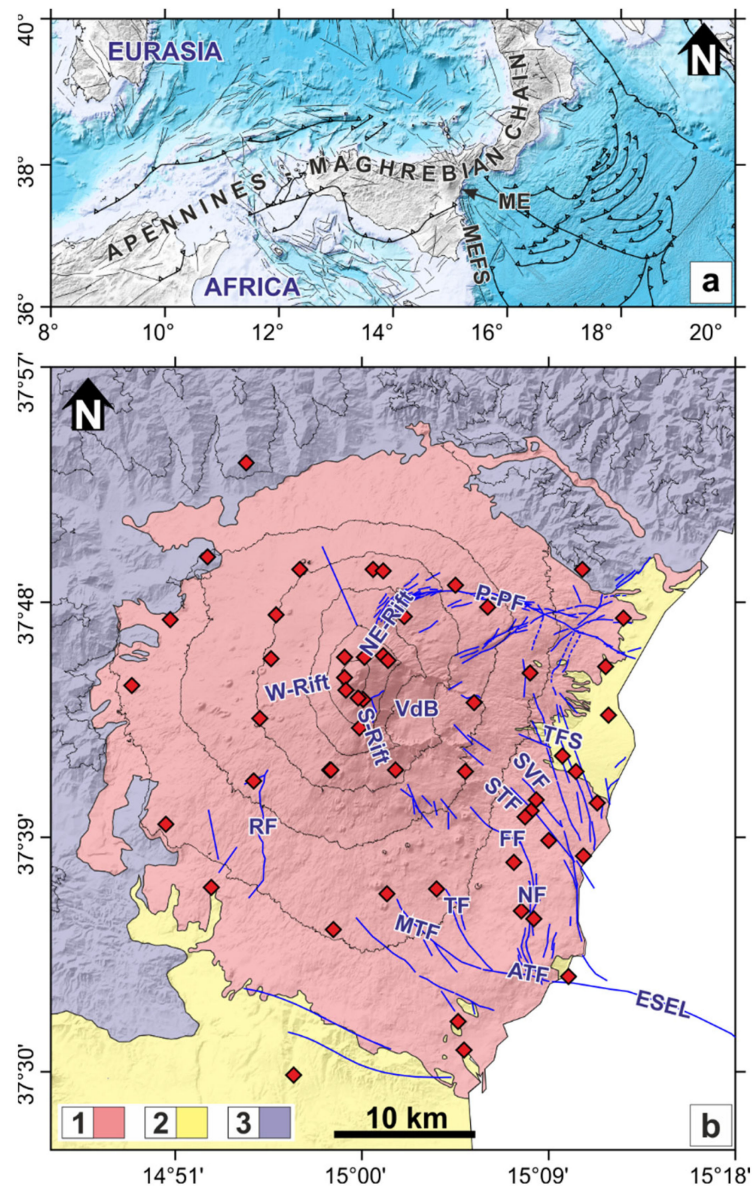


Figure 1. (a) Tectonic map of central Mediterranean. Abbreviations are: ME, Mt. Etna; MEFS, Malta Escarpment fault system. (b) Simplified geologic map of Mt. Etna. Legend: (1) volcanic rocks; (2) Early Quaternary clays; (3) Pre-Quaternary sedimentary rocks. Continuous GNSS stations are reported as red diamonds. Abbreviations are as follows: NE-Rift, North-East Rift; W-Rift, Western Rift; SE-Rift, South-East Rift; P-PF, Provenzana-Pernicana fault; TFS, Timpe fault system; SVE, Santa Venerina fault; STF, Santa Tecla fault; FF, Fiandaca fault; NF, Nizzeti fault system; TF, Trecastagni fault; MTF, Mascalucia-Tremestieri fault; ATF, Aci Trezza fault; RF, Ragalna fault; ESEL, ESE lineament.

Long-term deformation studies have focused on the seaward motion and the complex fragmentation of the eastern flank [11,12]. The flank instability has been documented since the early 1990s and several hypotheses on the origin and the kinematic boundaries have been proposed in the literature [13–15]. Most of the recent studies have pointed out that a large sector of the eastern flank is subject to a seaward steady-state motion with the north-eastern portion moving faster than the south-eastern one. However, other authors suggest that the southern flank is also affected by gravitational instability, so that the overall unstable sector covers an onshore area of $\sim 700 \text{ km}^2$ comprised between the Pernicana fault, to the north, and the Ragalna fault, to the south [13,16] (Figure 1b). The steady-state seaward motion is also modulated at different spatial and temporal scales by

other sources such as vigorous inflation/deflation episodes [6,7], fault creeping [17,18], and large-scale post-intrusion deformations [5,19].

The impressive December 2018 dike intrusion and associated volcanic activity led, two days after, to a M4.9 shallow earthquake on the south-eastern flank of the volcano and to a vigorous acceleration of the unstable flank, therefore representing a study case of an intrusion-flank motion in active volcanoes [1].

To fully define this spectacular modulation both in space and time, we analyzed a set of InSAR and GNSS data spanning the January 2015–April 2021 period, across the December 2018 paroxysmal episode, to clarify how remarkable short-time episodes interact with the overall deformation pattern of the volcano. In the first step, we analyzed both InSAR and GNSS data to obtain a ground displacement time-series for the entire investigated time interval. In a successive step, the whole investigated period was subdivided into four different time intervals and for each of them, the surface velocity field was estimated. Finally, the achieved results are discussed in the general volcanic and tectonic settings of the volcano.

2. Background Setting

The present-day shape of the Mediterranean region is the result of the long-lasting interaction (at least, since the Paleogene time) and collision between the Eurasia (to the north) and Africa (to the south) plates which led to the subduction and consumption of old oceanic basins (Tethys) and to the development of the circum-Mediterranean Alpine belt [20]. Subduction along the Eurasia–Africa plate boundary has progressively ceased due to the intervening continent–continent collision and currently is documented only beneath the Calabrian (Figure 1a) and the Hellenic arcs [20]. Convergence between Africa and Eurasia is still ongoing, and at the longitude of Sicily, it is occurring toward NW at rates of ~ 5 mm/yr [21].

Mt. Etna is a Quaternary composite basaltic volcano located on the hanging wall of the Apennine-Maghrebian accretionary wedge at the convergent margin between Eurasia and Africa plates (Figure 1a) on eastern Sicily [22,23]. Mt. Etna lies on a sedimentary basement (Figure 1b) formed by Miocene turbiditic deposits of the Apennines-Maghrebian chain and by early-middle Pleistocene foredeep marly clays [24]. Volcanic activity started about 500 ka ago as inferred by the shallow subvolcanic rocks intercalated in the top of the foredeep sediments [25]. The origin of this volcanism is debated and is currently explained by two contrasting hypotheses: (1) a passive asthenospheric mantle upwelling through a lithospheric tearing occurring at the south-western edge of the Calabrian subduction system [22,23] and (2) a laterally feeding mechanism from a melt pooling region located below the Malta Escarpment fault system [26]. The early stage of volcanism occurred as discontinuous and scattered submarine eruptive activity which progressively renewed through fissure-type eruptions in a subaerial environment in response to a regional uplift of north-eastern Sicily [25]. The fissure-type eruptions took place in a wide area corresponding to the present-day lower western and south-eastern flanks of the volcano edifice since 330 ka and 220 ka, respectively, leading to the formation of a primitive shield volcano structure [27]. Since 129 ka ago, the major eruptive centers progressively migrated towards the present-day Valle del Bove [28], favoring between 110 ka and 60 ka the formation of the earlier stratovolcano structure [29]. About 60 ka ago, eruptive activity shifted closely to the present-day eruptive centers along with the emplacement of wide lava fields which gradually expanded on the sedimentary basement [24]. The occurrence of several Plinian eruptions between 15 and 15.5 ka ago formed a wide summit caldera [30] over which a thick succession of superposed simple and compound lava flows and pyroclastic successions piled up in the last 15 ka. Around 10 ka ago, the wide depression of the Valle del Bove (Figure 1b) formed in response to a large gravitational slope failure of the eastern flank of the volcano [31]. In the last 10 ka, the occurrence of both effusive and largely explosive volcanic activity, ranging from frequent activity at the summit craters and episodic flank eruptions along radial fissures, led to the formation of three main rift zones [32], to the

west, south, and to the north-east (Figure 1b). In historical time, the volcanic activity has been discontinuously documented by Greek and Roman literature, while after the large 1669 eruption, a continuous production of documents and reports, coupled with an increase in quality and completeness of information, was carried out [33].

Nowadays, Mt. Etna has a central conduit, with five active summit craters located immediately westward of the Valle del Bove depression and is characterized by a quasi-steady-state seaward motion of its eastern flank (Figure 1b). This unstable sector is defined by a 25 km-wide horseshoe-shaped region delimited by the “North-East Rift-Provenzana-Pernicana fault system” to the north-east and by the “South Rift-Mascalucia-Tremestieri-Aci Trezza fault system” to the south-east (Figure 1b). Furthermore, active tectonics also occur over the unstable sector along several shallow faults such as the Timpe (TFS), the Santa Tecla (STF), the Santa Venerina (SVF), the Fiandaca (FF) and the Nizzeti (NF) ones [34] (Figure 1b).

Historical seismicity at Mount Etna has been well documented since 1633 [35] with numerous $M > 3.5$ earthquakes located on the active faults cutting the eastern flank. The strongest earthquake (estimated magnitude of 5.2) occurred on 8 May 1914 along the Santa Tecla fault. Instrumental seismicity, recorded since 2000 [36], mainly clustered beneath the summit area and the upper portions of the southern and eastern flanks, defining a large seismogenic volume extending down to the depth of ~10 km. Seismic events accompanying the major intrusive events of the last two decades concentrate within the shallow portion of this seismogenic volume, while the largest recorded earthquake occurred on 26 December 2018 on the Fiandaca fault, and was characterized by a very shallow focal depth (~2 km). Seismicity occurring along the Provenzana-Pernicana fault system is characterized by shallow depth (~2 km b.s.l.), occasionally reaching magnitude values larger than 3.5 [36]. Seismicity beneath the north-western flank is scant at shallow depths and abundant at depths larger than 20 km.

During the analyzed time interval, after the short-lived effusive eruption of 31 January to 2 February 2015 from the New South-East Crater (NSEC), the activity moved at the Voragine Crater where, on December 2015 and May 2016, it gave rise to a set of energetic paroxysmal eruptions [37]. After a period characterized by sporadic short-lived volcanic activity, intermittent lava emissions resumed again at the NSEC during February–April 2017. After about 15 months of rest, weak explosive activity resumed at the Bocca Nuova and North-East craters in July 2018, culminating with a modest effusive activity in late August 2018. An abrupt dike intrusion, accompanied by a seismic swarm with thousands of shallow events localized below the summit area and the upper south-eastern flank of the volcano took place on early 24 December 2018 [38]. The intrusion led to the formation of an eruptive fissure on the eastern side of the NSEC cone, which fed a short-lived lava flow directed into the Valle del Bove and propagated south-eastward for about 3 km [37]. On 26 December 2018, a M4.9 shallow earthquake struck the Fiandaca fault on the south-eastern flank of the volcano (Figure 1b), heavily damaging the towns and villages of the area [39]. In the following months, sporadic effusive/explosive events, such as the May–June 2019, July 2019, December 2019, April–May 2020 and December 2020 events, occurred at NSEC, and sometimes were accompanied by strombolian activity also at the Voragine Crater [40]. From 16 February up to the end of March 2021, a sequence of 17 vigorous lava fountain episodes took place at NSEC (see the weekly INGV monitoring reports at <https://www.ct.ingv.it/index.php/monitoraggio-e-sorveglianza/prodotti-del-monitoraggio/bollettini-settimanali-multidisciplinari>, accessed on 16 December 2021).

3. Ground Deformation Studies at Mt. Etna

The exploitation of different InSAR and GNSS datasets has allowed for extensive studies of surface deformation at Mt. Etna, providing evidence of how it responds to concurrent volcanic, tectonic, and gravitational processes. The most impressive deformations are mainly related to intrusive events, inflation/deflation cycles, and the seaward motion of the eastern flank. Vigorous deformations have been measured for all the intrusive

episodes occurred in the last two decades, i.e., the July–August 2001 [3,37–39,41,42], October 2002 [2], May 2008 [6], December 2014 [4,43], and December 2018 [5,44,45]. Inferred models have provided new insights on the shallow plumbing system, highlighting how the final kilometers of the magma upraise is controlled by a dominant E-W-oriented extension induced/modulated by the seaward motion of the eastern flank.

Relevant deformations have been measured also during the inflation/deflation cycles, characterizing the volcano activity of the last three decades. In particular, after the long-lasting inflation preceding the 2001 eruption [46], other numerous inflation/deflation cycles, with different durations, have been documented for Mt. Etna. These cycles are related to lava emission which can be also fed by shallow intrusions [2,4–6,42], silent/passive magma rising [7], and/or moderate-to-violent lava fountaining sequences [8,47]. Geodetic studies have greatly improved the knowledge on the plumbing system of the volcano, highlighting its multi-layered nature with different levels of magma accumulation.

The steady-state seaward motion of Mt. Etna's eastern flank also led to relevant wide-scale deformation. Such a motion has been geologically documented since the early 1990s [13]. The first GNSS-based measurements were carried out in 1997 on a small geodetic network installed across the Pernicana Fault [48], while Borgia et al. [14] and Froger et al. [49] highlighted significant deformation on some fault segments along the south-eastern flank of the volcano by exploiting a set of ERS1 interferometric images covering the 1992–1999 period. Multitemporal InSAR data processing methods, regarding a large stack of ERS1 and ERS2 interferograms, were firstly proposed by Lundgren et al. [50] to reveal the average and time-varying surface deformation at Mt. Etna from 1992 to 2001, largely improving the previous SAR studies based on single-pair interferometry [14,37,51]. Since then, the growing availability of extensive SAR datasets along with the continuous development of InSAR data processing techniques [52,53] has allowed us to achieve additional insights on inflation/deflation cycles and related active magmatic sources as well as geometry and kinematics of some blocks dissecting the unstable flank of the volcano [11,12,54]. A direct link between volcanic activity and the seaward motion has been hypothesized by several studies [11,13,15,24,42,54–61] and confirmed by analogical models [62]. Beside the volcanic activity, other different sources/mechanisms (e.g., faults creeping, co-seismic displacements, intrusive episodes, post-eruption relaxation) modulate at different spatial and temporal scales its continuous seaward motion [63]. For instance, horizontal rates from ~33 mm/yr to ~61 mm/yr have been estimated for the 2003–2015 period for the south-eastern and northern boundary of the eastern flank, respectively [64]. Horizontal rates of ~28 mm/yr have been geodetically estimated during the 1997–2001 period [17] along the Pernicana fault, which are slightly larger than the values estimated historically [65] and about an order of magnitude higher than the ones estimated from geological data [34]. The northern sector of the unstable flank has been characterized by the highest deformation rates, while most of the detected slow slip events at Mt. Etna concentrate both on the south-eastern sector of the eastern flank [63] as well as along offshore tectonic structures, e.g., the ESE-oriented tectonic lineament [66] (Figure 1b).

4. Geodetic Data

We analyzed a set of InSAR and GNSS data spanning the January 2015–April 2021 period, encompassing both the magmatic and seismic activities of December 2018 and the February–March 2021 lava fountain sequence. Taking into account these vigorous volcanic activities, as well as the general patterns of deformation, we subdivided the whole investigated period into four different time intervals (Figure 2): T1 from 18 January 2015 to 22 December 2018, T2 from 28 December 2018 to 2 June 2019, T3 from 2 June 2019 to 15 February 2021, and T4 from 15 February 2021–4 April 2021. The sharp displacement observed during the 22–28 December 2018 paroxysm (Figure S1) has been excluded by the computation of long-term velocities in T1 and T2.

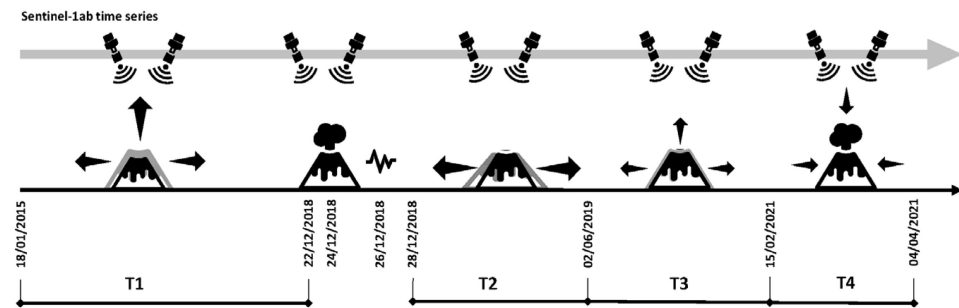


Figure 2. Timeline cartoon reporting the main deforming events and periods, from T1 to T4, as described in the main text.

The analyzed SAR dataset consists of two ascending and descending stacks of radar images acquired from the Sentinel-1A satellite operated by the European Space Agency and acquired in the TOPSAR mode (<https://search.asf.alaska.edu> (accessed on 30 January 2023)). We applied the Small Baseline Subset (SBAS) multitemporal method [53] to obtain ground displacement time-series and relative mean velocity maps. SBAS is one of the multitemporal interferometric SAR (MT-InSAR) techniques that use several interferograms obtained by pairing SAR images following specific spatiotemporal constraints. Differently to other MT-InSAR techniques, SBAS performs the analysis on natural distributed targets, permitting the maximum spatial coverage of the results. Here, data processing was performed by using the SARscape software by SARmap (sarmap SA, 5.6 version), implemented in the ENVI® (L3HARRIS) environment. Data processing was performed considering 182 and 186 images along the descending orbit (track 124) from 18 January 2015 to 4 April 2021 and the ascending orbit (track 44) during the 12 January 2015–29 March 2021 period, respectively. In order to generate the interferograms, we set the following spatiotemporal constraints: (i) orbital separation (spatial baseline) not exceeding 220 m to reduce spatial decorrelation; (ii) maximum temporal distance between the two satellite passes (temporal baseline) of 48 days to limit the effects of temporal decorrelation. A multilooking operation of 3 and 1 was, respectively, applied for the range and azimuth direction, to obtain a final ground resolution of 15 m useful for preserving the spatial details of displacement patterns. In the post-processing analysis, the mean ground velocity maps and relative time-series have been averaged on a 100×100 m grid in order to increase the signal-to-noise ratio and to ease the analysis of long spatial wavelength deformation signals.

During SBAS processing, the 30 m ALOS DEM (<https://www.eorc.jaxa.jp/ALOS/en/aw3d30/data/index.htm> (accessed on 30 January 2023)) was adopted as the reference elevation data to remove the topographic phase component from the interferograms. The filtering approach used in both elaborations is an extension of the Goldstein method [67] and was applied to remove the interferometric noise and enhance the interferometric fringes defining the ground deformation patterns. The Delaunay MCF unwrapping method was used in the processing. Points below a coherence threshold of 0.3 have not been unwrapped. The inversion of the interferometric phase was carried out using the Singular Value Decomposition algorithm, and the atmosphere phase contribution was estimated and removed, applying a double filtering in space and time, in order to correctly reconstruct the surface motion at each considered date along with the resulting displacement rate. Ascending and descending geometry velocity maps for (along the respective Line of Sight) T1 to T4 time intervals, as defined before, are shown in Figures 3 and 4.

Finally, the availability of both ascending and descending acquisition geometries allowed us to calculate the nearly horizontal (east–west) and nearly vertical components of the displacement (Figures 5 and 6) during the time period covered by both Line of Sight (LoS) elaborations [68] as well. Additionally, in this case, as performed for ascending and descending dataset results, east–west and vertical components products have been subsampled at 100 m resolution mesh. Precisions for LoS and cartesian velocities [69] are calculated as reported in the Supplementary Materials (Figure S2).

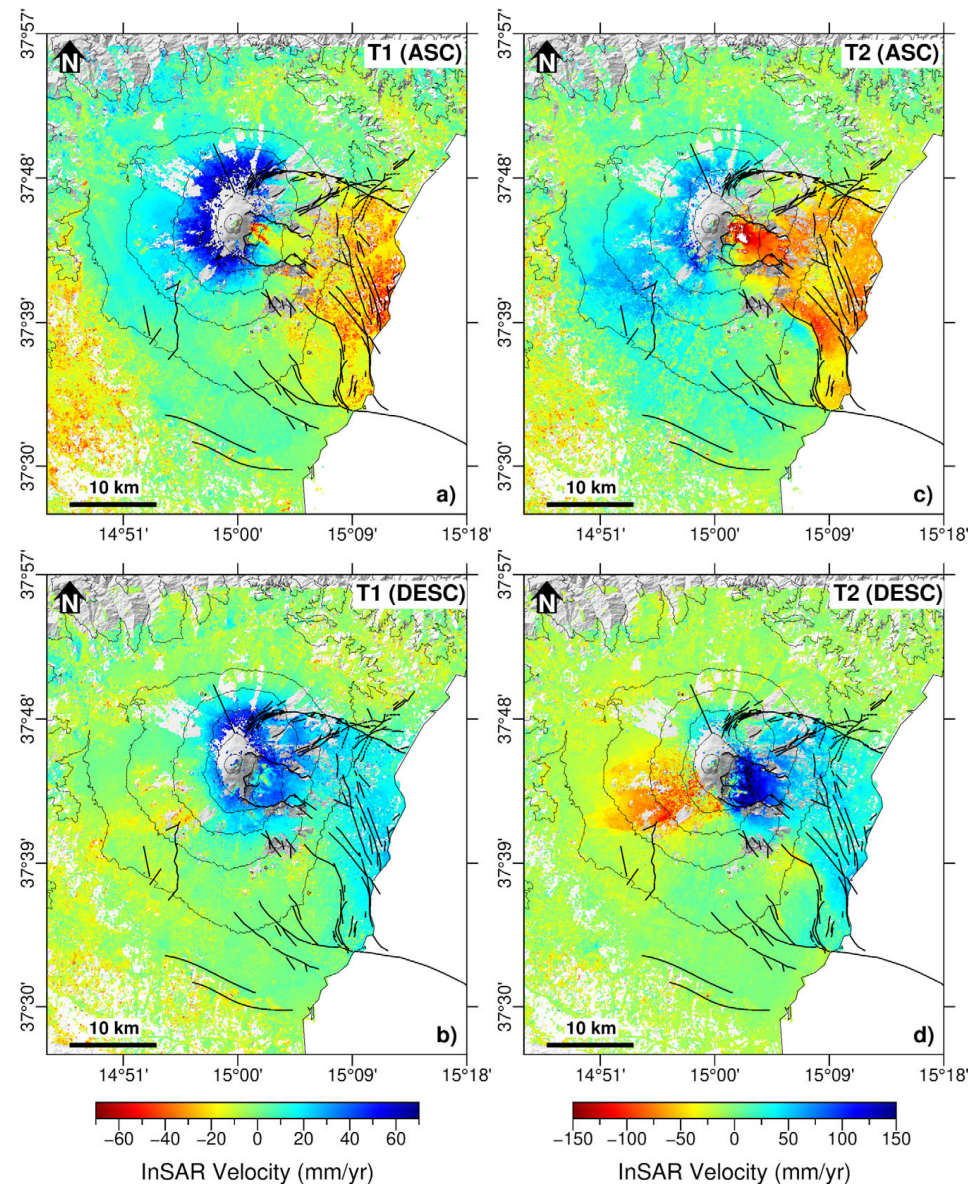


Figure 3. Ascending (panels a,c) and descending (panels b,d) LoS velocity maps relative to T1 (18 January 2015–22 December 2018) and T2 (28 December 2018–2 June 2019) time intervals. Positive values (blue colors) represent scatterers approaching the satellite, negative values (red colors) are moving away. Main faults are also reported as black lines.

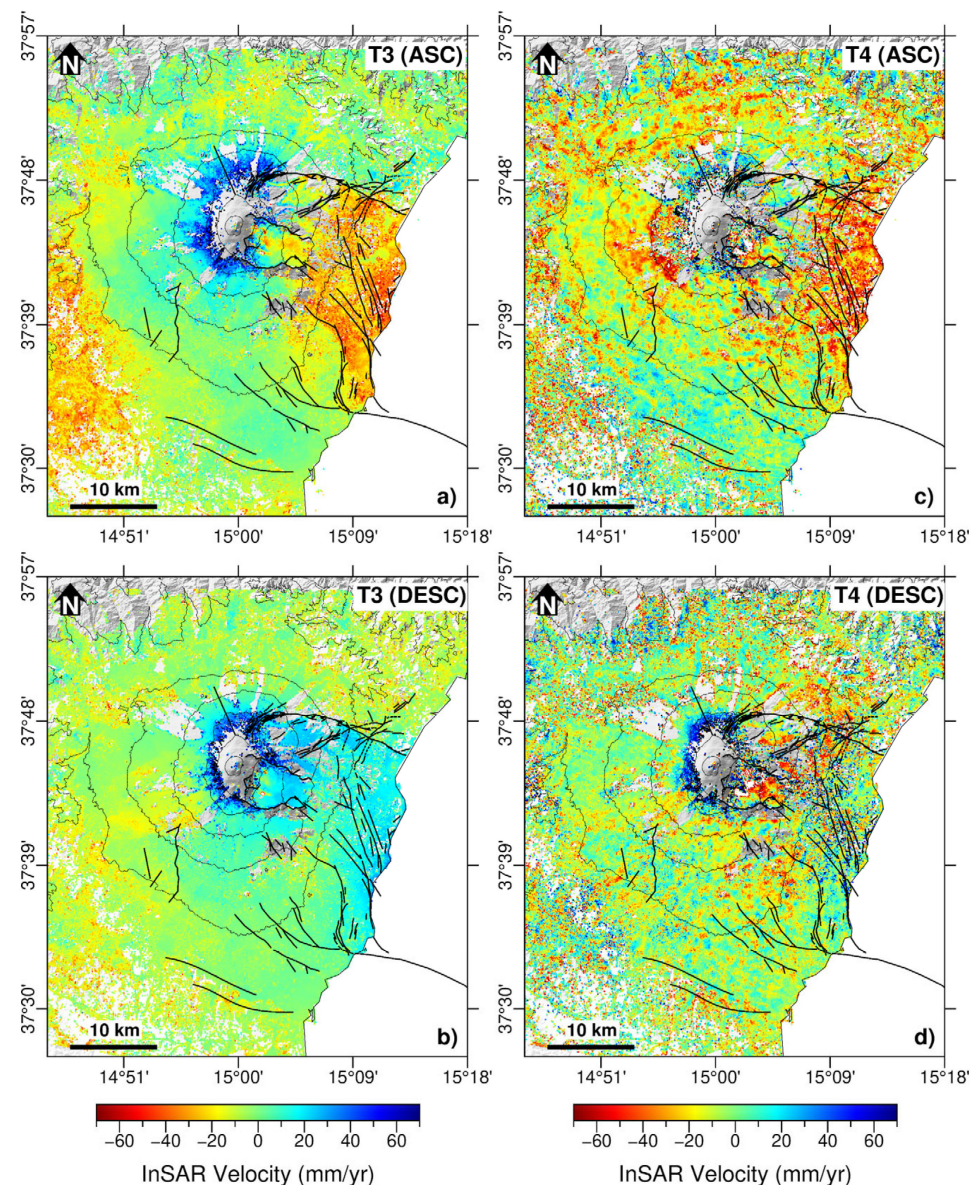


Figure 4. Ascending (panels **a,c**) and descending (panels **b,d**) velocity maps relative to T3 (2 June 2019–15 February 2021) and T4 (15 February 2021–29 March 2021) time intervals. Positive values (blue colors) represent scatterers approaching the satellite, negative values (red colors) are moving away. Main faults are also reported as black lines.

All collected raw GNSS observations, spanning the January 2015–April 2021 period, were processed by using the GAMIT/GLOBK software [70] and by taking into account precise ephemerides from the IGS (International GNSS Service; <http://igsceb.jpl.nasa.gov> (accessed on 30 January 2023)) and Earth orientation parameters from the International Earth Rotation Service (<http://www.iers.org> (accessed on 30 January 2023)). To improve the overall configuration of the network and tie the regional measurements to an external global reference frame, data coming from 15 continuously operating IGS stations were introduced in the processing. We used the latest absolute receiver antenna models by the IGS and we adopted the Saastamoinen [71] atmospheric zenith delay models, coupled with the Global Mapping Functions [72] for the neutral atmosphere. Estimated velocity fields for each of the four time intervals previously identified were referred to a local reference frame [63]. Achieved results are reported in Figures 5 and 6.

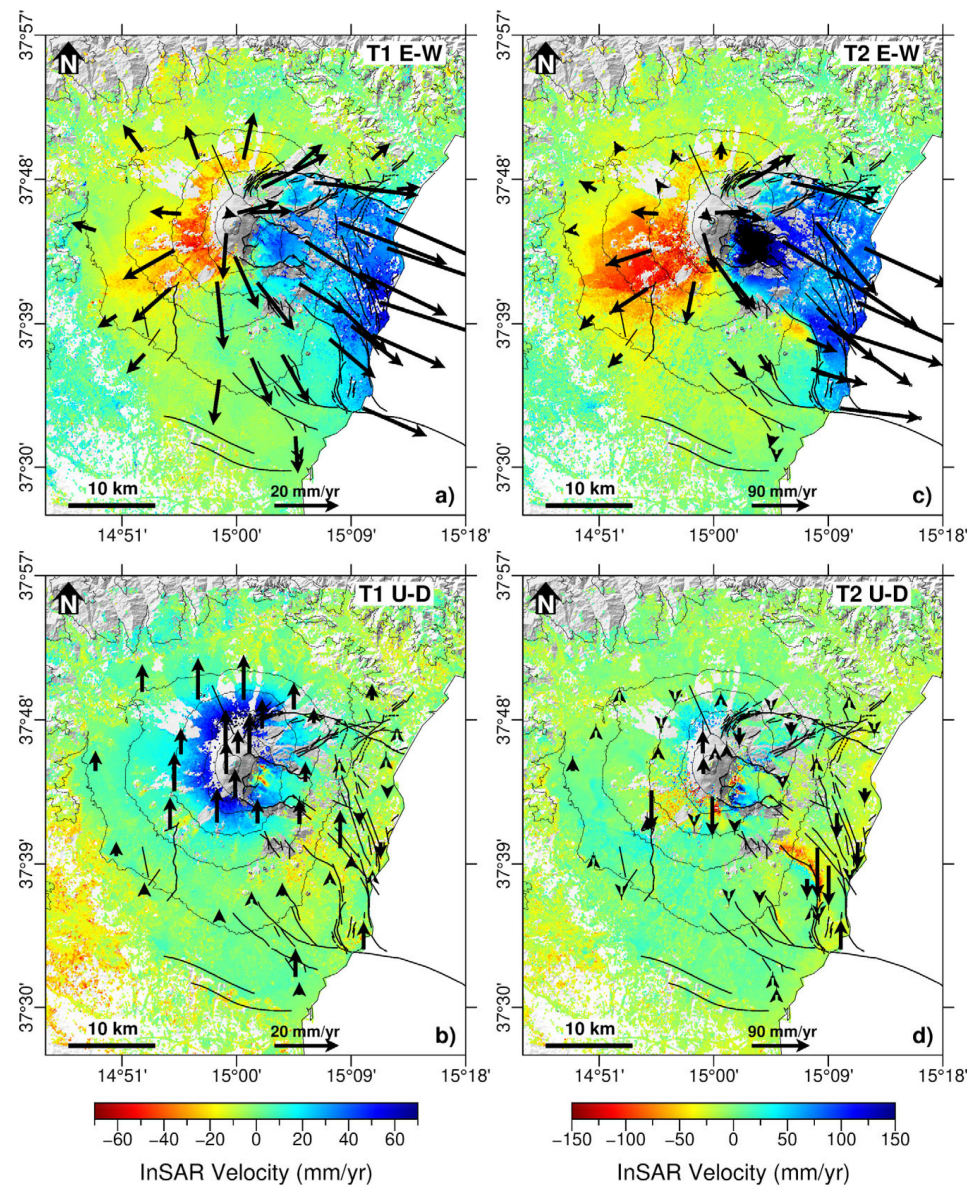


Figure 5. Horizontal (panels a,c) and vertical (panels b,d) component velocity maps relative to T1 (18 January 2015–22 December 2018) and T2 (28 December 2018–2 June 2019) time intervals. Positive values (blue colors) represent scatterers eastward in panels (a,c); and uplifting in panels (b,d). Negative values (red colors) are moving westward in panels (a,c), and subsiding in panels (b,d). GNSS velocity vectors of the horizontal and vertical components relative to the same time period are reported for each panel as black arrows.

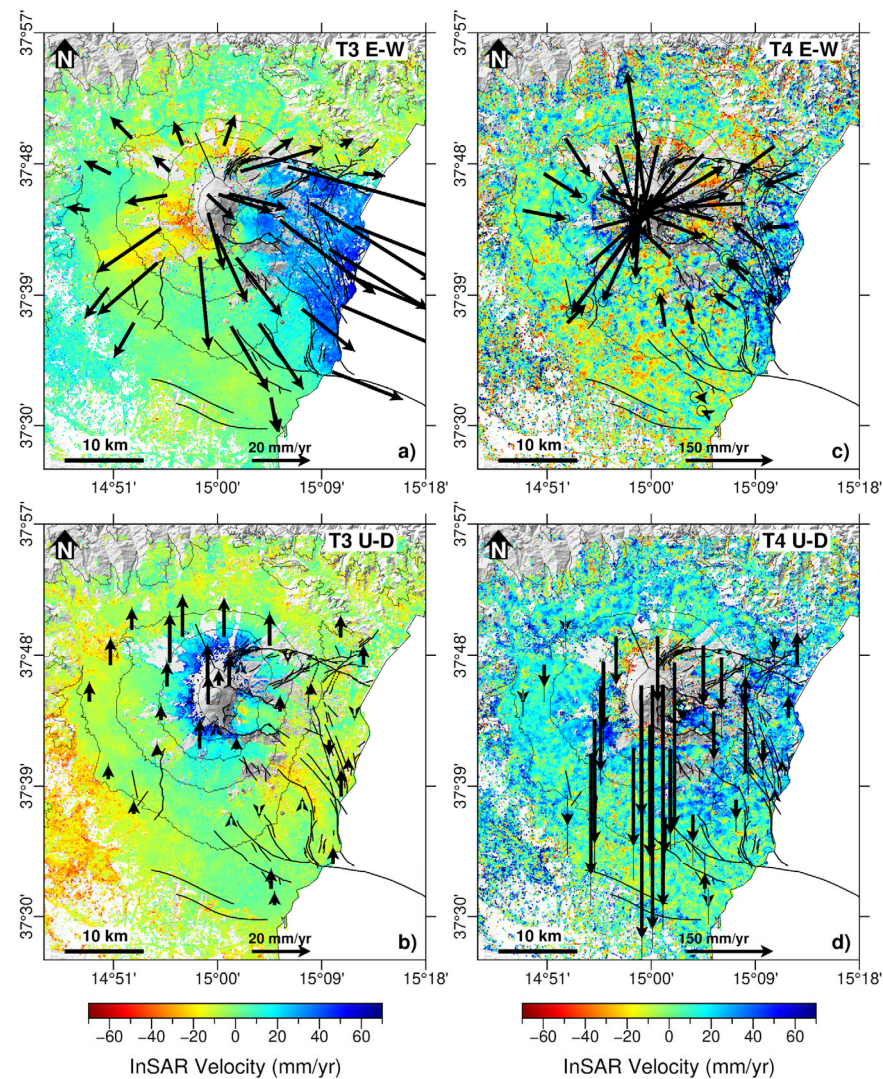


Figure 6. Horizontal (panels **a,c**) and vertical (panels **b,d**) component velocity maps relative to T3 (2 June 2019–15 February 2021) and T4 (15 February 2021–29 March 2021) time intervals. Positive values (blue colors) represent scatterers eastward in panels (**a,c**); and uplifting in panels (**b,d**). Negative values (red colors) are moving westward in panels (**a,c**), and subsiding in panels (**b,d**). GNSS velocity vectors of the horizontal and vertical components relative to the same time period are reported for each panel as black arrows.

5. Results

GNSS and InSAR deformation fields estimated for the four time intervals coherently define a high variability of patterns in response to the different volcanic and seismic activities occurring at Mt. Etna through the January 2015–March 2021 period. Moreover, deformations in the summit area and in the eastern flank are of paramount relevance throughout the analyzed period.

During T1 (18 January 2015–22 December 2018; Figure 5a,b), the volcano edifice is subject to a general inflation with uplift reaching about 70 mm/yr (from the InSAR dataset) in the summit area. This deformation pattern is reasonably ascribable to melt rising along the plumbing system of the volcano, in agreement with the long-lasting inflation phase started since early 2015, episodically interrupted by small deflations related to short-term volcanic activities [10,35,47]. The deformation on the eastern flank is mainly confined between the Provenzana-Pernicana fault system, to the north, and the tectonic arrangement defined by the Fiandaca, Nizzeti and Aci Trezza faults, to the south, with horizontal rates of

35 mm/yr, on average (Figure 5a,b). During this time interval, deformations of ~5 mm/yr can be recognized also along the Mascalucia-Tremestieri fault system.

During T2 (28 December 2018–27 May 2019; Figure 5c,d), the scene is dominated by large deformations involving the upper western flank, the summit area, and the eastern flank, in response to the magmatic intrusion which occurred on 24 December beneath the summit area and the M4.9 shallow earthquake which occurred on 26 December along the Fiandaca fault [5]. On the upper western flank and the summit area, the deformation field is characterized by horizontal values up to 100 mm/yr, while the vertical pattern shows a modest uplift (up to 30 mm/yr), with some localized patches of subsidence (Figure 5d). Such a pattern would reflect a general restoring of the plumbing system of the volcano with the magmatic replenishment of the reservoir feeding the 24 December 2018 volcanic activity [5]. On the eastern flank, the prevalent deformation pattern remarks the main features observed during T1, with the exception that horizontal rates drastically increased up to 160 mm/yr. Again, small deformations can be recognized during this time interval along the Mascalucia-Tremestieri fault system.

Deformation which occurred during the T3 period (2 June 2019–15 February 2021; Figure 6a,b) dropped to values similar to the ones already observed during T1. In particular, the summit area and the upper western flank exhibit an uplift up to 25 mm/yr coupled with an asymmetric radial pattern with values ranging from ~10 mm/yr (northward and north-westward the summit area) to ~30 mm/yr (upper western and south-western flanks). This pattern would reflect an inflation of the volcano which, however, is causing a prevalent horizontal growth of the edifice. Regarding the eastern flank, the northern portion moves toward the sea with horizontal rates of ~50 mm/yr, while the southern one moves with rates of ~30 mm/yr. The most deforming area is mainly confined between the same tectonic elements defined in T1.

T4 (15 February 2021–29 March 2021) covers a short time interval characterized by intense explosive activity with the occurrence of 17 lava fountaining episodes at the NSEC. The estimated InSAR velocity fields for both E-W (Figure 6c) and vertical (Figure 6d) components are poorly constrained and noisy, probably due to the incomplete atmospheric estimation and removal in the last processed SAR acquisitions. Conversely, the horizontal GNSS velocity field (Figure 6c) describes a centripetal pattern clearly capturing a general deflation of the whole volcano edifice. Such a general deflation is also confirmed by the vertical GNSS velocity field (Figure 6d). The highest deformation is confined to the summit area with rates up to 280 mm/yr and 400 mm/yr for the horizontal and vertical components, respectively. On the lower eastern flank, the GNSS stations show a westward pattern, which overread the long-term steady-state seaward motion, and suggest a deep and vigorous depressurizing source.

The achieved InSAR and GNSS results led to some relevant considerations, especially taking into account T1, T2, and T3 time intervals. Both GNSS and InSAR E-W component velocities on the eastern volcano flank show large variability during the three time intervals. In T1, the unstable flank moves eastward with high velocity clusters on the summit and along the coastal belt. These double velocity picks are related to the simultaneous action of at least two main processes: (1) the magma movements along the plumbing system, responsible for high eastward velocity pick in the summit area; (2) a gravitational traction of the eastern flank highlighted by the increase in ground velocities moving eastward from the summit area of the volcano.

The western flank exhibits a general western to south-western motion over all T1, T2 and T3 time intervals, with a consistent increase in velocity values during T2, in response to the December 2018 shallow intrusion. The high velocity pattern observed in T2 involves a large portion of the western flank, while during T3, it drastically slowed down and was observed only on its upper portion. This pattern, coupled with the small velocity values observed during the overall investigated time interval on the lower western flank, floors the interpretation of the western flank displacement as related to a placing of magma instead of a gravity-driven process.

The northern slope relatively moves westward in both T1 and T3 periods, characterized by low-intensity volcanic activity. Specularly, the southern slope (excluding the portion involved in the seaward sliding) is characterized by slow eastward movements. Thus, despite the misrepresentation of north–south displacements in InSAR data processing, the deformation pattern implies that the northern and southern flanks are partially coupled to the western and eastern flanks, respectively, but with significantly smaller movements. Moreover, the relatively small GNSS velocities along the slope directions lend credit to the interpretation that gravity is not the major cause of deformation in the north and south slopes of the volcano. On the other hand, the overall picture of east velocities in T1 and T2 periods returns a WNW-ESE-oriented spreading characterized by a long spatial wavelength and hinged along an NNE-SSW axis.

6. Discussion

The analyzed InSAR and GNSS datasets capture some interesting features of the surface deformation of Mt. Etna volcano over the 2015–2021 time interval.

A primary feature is the near-continuous inflation of the volcano, as clearly observed in T1, T2, and T3 time intervals (Figures 5 and 6). Such a process is related to a prolonged replenishment of magma at different depths and with different rates along the plumbing system of the volcano, with some episodes described in previous studies [5,37,40,44]. The inflation observed during T1 (Figure 5a,b) has led to the fast intrusive episode and the vigorous volcanic activity of December 2018, while the inflation observed during T2 and T3 (Figures 5b,c and 6a,b) culminated in T4 with the February–March 2021 lava fountain sequence, which in turn provoked a fast short-term deflation of the entire volcano edifice (Figure 6c,d). Considering the geodetic models reported by Viccaro et al. [10] and Borzi et al. [37], the inflation which occurred during T1 was characterized by a magma accumulation ($\sim 40 \times 10^6 \text{ m}^3$ in total, as geodetically estimated), of which is the largest magma accumulation that has occurred in the last 15 years. Conversely, the inflations observed during T2 and T3, although occurring at different rates [40], are characterized by smaller values ($\sim 11 \times 10^6 \text{ m}^3$ in total, as geodetically estimated), close to those more commonly observed at Mt. Etna [6–8,73].

Moreover, the onset of a large magma accumulation, culminating with fast and vigorous intrusive episodes, has been already observed, at least before the 2001 and 2002–2003 eruptions. In particular, the 2001 eruption was preceded by a long-lasting inflation that started in 1993 [46] and a sharp increase in seismicity [74], while the 2002–2003 eruption was preceded by a one-year-long vigorous inflation [9]. The onset of both the 2001 and 2002–2003 eruptions led also to accelerations of the eastern flank seaward motion, with small values measured along the Pernicana fault after the 2001 eruption [17] and remarkable values, coupled with significant shallow seismic activity which spread on the eastern flank after the 2002–2003 eruption [19,51,57]. The ground deformation patterns encompassing the December 2018 paroxysm share several similarities with the ones observed during and after the 2001 and 2002–2003 intrusions. The linked sequence of vigorous lateral intrusion and acceleration of the seaward flank motion due to large accumulation of magma defines an “exceptional” behavior of the volcano. This behavior deviates from the more “common” one consisting of small-to-moderate inflation episodes feeding explosive/effusive activity with very small modulations of the seaward eastern flank motion. A major discriminant element between the two behaviors seems to be the quantity of magma accumulating beneath the volcano. Only large magma accumulations appear to culminate with the “exceptional” behavior, the early recognition of which could be relevant to help forecasting the volcanic activity.

After the December 2018 paroxysm, the abrupt acceleration of the seaward motion of the eastern flank is well impressed in geodetic data (T2; Figure 5a,b). The process is driven by an ambient stress perturbation in response to the lateral push of magma rising along the shallow intrusion pathway, which also favored the recrudescence of seismic activity on the faults cutting/bordering the unstable flank [5,38]. The abrupt

acceleration does not homogeneously involve the whole eastern flank, but only the sector delimited by the Provenzana-Pernicana fault system to the north, and by the Fiandaca, Nizzeti and Aci Trezza faults to the south. In addition, just after the intrusion onset, east velocities of the unstable sector (see Figure 3 in Pezzo et al. [5] 2020 for details) followed an exponential decay, similar to the one already observed the days after the October 2002 intrusion onset [19]. We observed two distinct patches of high velocities on the summit area of the volcano and along the coastal sector of the unstable flank in T1, and a general eastward-increasing velocity in T2. The T3 pattern is similar to the T1 one with slightly higher values. In T4, the whole eastern flank reversed its motion, with a westward pattern and rates that increased from the coastal to the summit area. This reversal clearly indicates that the short-term contraction of the volcano occasionally overcomes the gravity-controlled sliding of the eastern flank. Shallow dike intrusions generally induce an acceleration of the flank sliding, while vigorous deflation led to a deceleration. Decelerations of the eastern flank seaward motion did not pose particular hazard problems to the towns and villages of the area; conversely, rapid flank acceleration could potentially evolve into sudden collapses, accelerated fault creeping, and seismic release at shallow depths, therefore leading to significant hazard scenarios.

We observed that the flank sliding is accommodated differently at its edges. To the north, the seaward motion is confined along the Provenzana-Pernicana fault system (Figures 5 and 6), whose displacement is mainly characterized by aseismic creep, with sporadic low-moderate magnitude seismicity [34]. To the south, the flank motion is accommodated by different faults within a ~10 km broad zone (Figure 1b), as clearly evidenced by our analyzed GNSS and InSAR datasets. This difference is probably related to the presence of heterogeneities in the shallow portion of the basement. The localization of deformation on the Provenzana-Pernicana fault system and its creeping behavior is reasonably related to a higher temperature present in the volcanic cover and basement, with respect to that on the southern portion [38]. The faults here extend for a few kilometers in the basement and reasonably have more brittle behavior that can host higher magnitude events, like that of 2018.

On the western flank, the observed deformation seems related to the large-scale widening of the entire volcano edifice. Indeed, the observed acceleration from T1 to T2, and the subsequent deceleration in T3, coupled with relevant seismic activity (e.g., the October 2018 seismic swarm; $M_{max} = 4.7$) [34] and a relevant uplift, would suggest a deep magma injection, potentially able to feed peripheral dangerous eruptions.

7. Conclusions

The InSAR and GNSS present-day deformation at Mt. Etna volcano reveals a complex interaction between magma movements along the plumbing system, volcanic activity, and gravitational processes. Based on the achieved results, we derived the following conclusions:

(i) During the analyzed time interval, the gravity-controlled background seaward motion of the eastern flank was modulated by vigorous short-term volcanic activities such as a dike intrusion and a volcano-wide deflation.

(ii) The 2018 dike intrusion led to a sudden acceleration of the eastern flank, exponentially decaying in the following months.

(iii) The vigorous volcano-scale deflation observed during the short T4 time interval, characterized by the occurrence of 17 lava fountaining episodes at the NSEC, led to a westward motion of the eastern flank, overcoming its long-term gravity-controlled seaward sliding.

A sudden acceleration of the unstable flank has been observed also during/after the 2001 and 2002–2003 eruptions, while deceleration episodes related to vigorous deflations have been rarely documented. Moreover, these well-documented volcanic activity/flank collapse interactions can be of relevance for addressing short-term hazard scenarios, yielding tentative forecasts of the quantity of new magma replacements at shallow depths. This

lesson is documented at Mt. Etna and can be of global relevance for other stratovolcanoes with similar dynamics as Kilauea (USA) and Piton de la Fournaise (Reunions Islands).

Supplementary Materials: Supplementary text and figures can be downloaded at: <https://www.mdpi.com/article/10.3390/rs15030847/s1>. Figure S1: Sentinel-1 ascending (a) and descending (b) interferograms covering the 22–28 December 2018 period. The black arrows represent the horizontal (a) and the vertical (b) GNSS displacements measured during the same time interval. Figure S2: Ascending (upper left), descending (upper right), vertical (lower left) and horizontal (lower right) displacement precision maps. These outcomes, which are derived from parameters such as coherence and wavelength using the formula provided in [69], offer an estimation of the SAR results error. The higher the precision value, the lower the measurement precision. Figure S3: Example of GNSS and InSAR LOS displacement time-series for some selected stations. On the top: North, East and Up displacement time-series for GNSS (G) stations; on the bottom, to the right: InSAR (I) LOS displacement ascending (red) and descending (blue) time-series for points closer to the GNSS stations. The vertical blue and gray lines mark the shallow intrusions onset and the lava fountain episodes occurred in the analyzed time interval, respectively. On the bottom, to the left: location map of the selected stations/sites.

Author Contributions: Conceptualization, G.P., M.P. and C.C.; methodology, M.P., G.P., L.B., C.T., M.A., S.A. and C.C.; software, M.P., G.P., L.B., S.A. and C.T.; validation, M.P., L.B., C.T. and M.A.; formal analysis, M.P., G.P., L.B., S.A. and C.T.; investigation, M.P., G.P., L.B. and C.T.; data curation, M.P., L.B., G.P., S.A. and C.T.; writing—original draft preparation, G.P., M.P. and C.C.; writing—review and editing, L.B. and C.T.; visualization, M.P., L.B. and G.P.; supervision, C.C.; project administration, M.P., G.P. and C.C.; funding acquisition, M.P., G.P. and C.C. All authors have read and agreed to the published version of the manuscript.

Funding: This work is supported by the Project “Paroxysmal volcanic events and seaward motion at Mt. Etna: an improved picture from a geodetic and seismological perspective” (Progetti di Ricerca Libera) funded by INGV.

Data Availability Statement: Synthetic Aperture Radar (SAR) data used for deformation analysis are copyrighted by the European Space Agency and freely available at <https://search.asf.alaska.edu> (accessed on 30 January 2023). GNSS data used in this study are available from the corresponding author upon request.

Acknowledgments: Most of the figures were made using the GMT software (Wessel and Smith, 1998). We thank Daniele Pellegrino, Mario Pulvirenti and Massimo Rossi who ensured the maintenance and acquisition of the continuous GNSS stations.

Conflicts of Interest: The authors declare no conflict of interest.

References

1. Neal, C.A.; Brantley, S.R.; Antolik, L.; Babb, J.L.; Burgess, M.; Calles, K.; Cappos, M.; Chang, J.C.; Conway, S.; Desmither, L.; et al. The 2018 rift eruption and summit collapse of Kilauea Volcano. *Science* **2019**, *363*, 367–374. [[CrossRef](#)]
2. Aloisi, M.; Bonaccorso, A.; Gambino, S.; Mattia, M.; Puglisi, G. Etna 2002 eruption imaged from continuous tilt and GPS data. *Geophys. Res. Lett.* **2003**, *30*, 2214. [[CrossRef](#)]
3. González, P.J.; Palano, M. Mt. Etna 2001 eruption: New insights into the magmatic feeding system and the mechanical response of the western flank from a detailed geodetic dataset. *J. Volcanol. Geother. Res.* **2014**, *274*, 108–121. [[CrossRef](#)]
4. Gambino, S.; Cannata, A.; Cannavò, F.; La Spina, A.; Palano, M.; Sciotto, M.; Spampinato, L.; Barberi, G. The unusual 28 December 2014 dike-fed paroxysm at Mount Etna: Timing and mechanism from a multidisciplinary perspective. *J. Geophys. Res. Solid Earth* **2016**, *121*, 2037–2053. [[CrossRef](#)]
5. Pezzo, G.; Palano, M.; Tolomei, C.; De Gori, P.; Calcaterra, S.; Gambino, P.; Chiarabba, C. Flank sliding: A valve and a sentinel for paroxysmal eruptions and magma ascent at Mount Etna, Italy. *Geology* **2020**, *48*, 1077–1082. [[CrossRef](#)]
6. Aloisi, M.; Mattia, M.; Ferlito, C.; Palano, M.; Bruno, V.; Cannavò, F. Imaging the multi-level magma reservoir at Mt. Etna volcano (Italy). *Geophys. Res. Lett.* **2011**, *38*, L16306. [[CrossRef](#)]
7. Bruno, V.; Mattia, M.; Aloisi, M.; Palano, M.; Cannavò, F.; Holt, W. E. Ground deformations and volcanic processes as imaged by CGPS data at Mt. Etna (Italy) between 2003 and 2008. *J. Geophys. Res.* **2012**, *117*, B07208. [[CrossRef](#)]
8. Spampinato, L.; Sciotto, M.; Cannata, A.; Cannavò, F.; La Spina, A.; Palano, M.; Salerno, G.G.; Privitera, E.; Caltabiano, T. Multiparametric study of the February–April 2013 paroxysmal phase of Mt. Etna New South-East crater. *Geochem. Geophys. Geosyst.* **2015**, *16*, 1932–1949. [[CrossRef](#)]

9. Palano, M.; Viccaro, M.; Zuccarello, F.; Gresta, S. Magma transport and storage at Mt. Etna (Italy): A review of geodetic and petrological data for the 2002–03, 2004 and 2006 eruptions. *J. Volcanol. Geotherm. Res.* **2017**, *347*, 149–164. [[CrossRef](#)]
10. Viccaro, M.; Giuffrida, M.; Zuccarello, F.; Scandura, M.; Palano, M.; Gresta, S. Violent paroxysmal activity drives self-feeding magma replenishment at Mt. Etna. *Sci. Rep.* **2019**, *9*, 6717. [[CrossRef](#)]
11. Solaro, G.; Acocella, V.; Pepe, S.; Ruch, J.; Neri, M.; Sansosti, E. Anatomy of an unstable volcano from InSAR: Multiple processes affecting flank instability at Mt. Etna, 1994–2008. *J. Geophys. Res.* **2010**, *115*, B10405. [[CrossRef](#)]
12. Bonforte, A.; Guglielmino, F.; Coltelli, M.; Ferretti, A.; Puglisi, G. Structural assessment of Mount Etna volcano from Permanent Scatterers analysis. *Geochem. Geophys. Geosyst.* **2011**, *12*. [[CrossRef](#)]
13. Borgia, A.; Ferrari, L.; Pasquarè, G. Importance of gravitational spreading in the tectonic and volcanic evolution of Mount Etna. *Nature* **1992**, *357*, 231–235. [[CrossRef](#)]
14. Borgia, A.; Delaney, P.T.; Denlinger, R.P. Spreading volcanoes. *Ann. Rev. Earth Planet. Sci.* **2000**, *28*, 539–570. [[CrossRef](#)]
15. Ruch, J.; Acocella, V.; Storti, F.; Neri, M.; Pepe, S.; Solaro, G.; Sansosti, E. Detachment depth revealed by rollover deformation: An integrated approach at Mount Etna. *Geophys. Res. Lett.* **2010**, *37*, L16304. [[CrossRef](#)]
16. Rust, D.; Neri, M. The boundaries of large-scale collapse on the flanks of Mount Etna, Sicily. In *Volcano Instability on the Earth and Other Planets*; McGuire, W.M., Jones, A.P., Neuberg, J., Eds.; Geological Society of London: London, UK, 1996; Volume 110, pp. 193–208.
17. Palano, M.; Aloisi, M.; Amore, M.; Bonforte, A.; Calvagna, F.; Cantarero, M.; Consoli, O.; Guglielmino, F.; Mattia, M.; Puglisi, B.; et al. Kinematics and strain analyses of the eastern segment of the Pernicana fault (Mt. Etna, Italy) derived from geodetic techniques (1997–2005). *Ann. Geophys.* **2006**, *49*, 1105–1117. [[CrossRef](#)]
18. Gambino, S.; Bonforte, A.; Carnazzo, A.; Falzone, G.; Ferrari, F.; Ferro, A.; Guglielmino, F.; Laudani, G.; Maiolino, V.; Puglisi, G. Displacement across the Trecastagni Fault (Mt. Etna) and induced seismicity: The October 2009 to January 2010 episode. *Ann. Geophys.* **2011**, *54*, 414–423.
19. Palano, M.; Gresta, S.; Puglisi, G. Time-dependent deformation of the eastern flank of Mt. Etna: After-slip or viscoelastic relaxation? *Tectonophysics* **2009**, *473*, 300–311. [[CrossRef](#)]
20. Van Hinsbergen, D.J.; Torsvik, T.H.; Schmid, S.M.; Mañenco, L.C.; Maffione, M.; Vissers, R.L.; Gürer, D.; Spakman, W. Orogenic architecture of the Mediterranean region and kinematic reconstruction of its tectonic evolution since the Triassic. *Gondwana Res.* **2020**, *81*, 79–229.
21. Billi, A.; Cuffaro, M.; Orecchio, B.; Palano, M.; Presti, D.; Totaro, C. Retracing the Africa–Eurasia nascent convergent boundary in the Western Mediterranean based on earthquake and GNSS data. *Earth Planet. Sci. Lett.* **2023**, *601*, 117906. [[CrossRef](#)]
22. Gvirtzman, Z.; Nur, A. The formation of Mount Etna as the consequence of slab rollback. *Nature* **1999**, *401*, 782–785. [[CrossRef](#)]
23. Doglioni, C.; Innocenti, F.; Mariotti, G. Why Mt Etna? *Terra Nova* **2001**, *13*, 25–31. [[CrossRef](#)]
24. Branca, S.; Ferrara, V. The morphostructural setting of Mount Etna sedimentary basement (Italy): Implications for the geometry and volume of the volcano and its flank instability. *Tectonophysics* **2013**, *586*, 46–64. [[CrossRef](#)]
25. Di Stefano, A.; Branca, S. Long-term uplift rate of the Etna volcano basement (southern Italy) based on biochronological data from Pleistocene sediments. *Terra Nova* **2002**, *14*, 61–68. [[CrossRef](#)]
26. Neri, M.; Rivalta, E.; Maccaferri, F.; Acocella, V.; Cirrincione, R. Etnean and Hyblean volcanism shifted away from the Malta Escarpment by crustal stresses. *Earth Planet. Sci. Lett.* **2018**, *486*, 15–22. [[CrossRef](#)]
27. Branca, S.; Coltelli, M.; De Beni, E.; Wijbrans, J. Geological evolution of Mount Etna volcano (Italy) from earliest products until the first central volcanism; (between 500 and 100 ka ago) inferred from geochronological and stratigraphic data. *Int. J. Earth Sci.* **2008**, *97*, 135–152. [[CrossRef](#)]
28. Nicolosi, I.; D’Ajello Caracciolo, F.; Branca, S.; Ferlito, C.; Chiappini, M. The earliest open conduit eruptive center of the Etnean region: Evidence from aeromagnetic, geophysical, and geological data. *Bull. Volcanol.* **2016**, *78*, 50. [[CrossRef](#)]
29. De Beni, E.; Branca, S.; Coltelli, M.; Groppelli, G.; Wijbrans, J.R. ⁴⁰Ar/³⁹Ar isotopic dating of Etna volcanic succession. *It. J. Geosci. (Boll. Soc. Geol. It.)* **2011**, *130*, 292–305.
30. Coltelli, M.; Del Carlo, P.; Vezzoli, L. Stratigraphic constraints for explosive activity in the past 100 ka at Etna Volcano, Italy. *Int. J. Earth Sci.* **2000**, *89*, 665–677. [[CrossRef](#)]
31. Calvari, S.; Tanner, L.H.; Groppelli, G.; Norini, G. Valle del Bove, eastern flank of Etna volcano: A comprehensive model for the opening of the depression and implications for future hazards. In *Etna Volcano Laboratory*; Bonaccorso, A., Calvari, S., Coltelli, M., Del Negro, C., Falsaperla, S., Eds.; AGU Geophysical Monograph Series; American Geophysical Union: Washington, DC, USA, 2004; Volume 143, pp. 1–27.
32. Garduño, V.H.; Neri, M.; Pasquarè, G.; Borgia, A.; Tibaldi, A. Geology of the NE Rift of Mount Etna, Sicily (Italy). *Acta. Vulcanol.* **1997**, *9*, 91–100.
33. Branca, S.; Del Carlo, P. Eruptions of Mt Etna during the past 3200 years: A revised compilation integrating the Historical and stratigraphic records. In *Mt. Etna: Volcano laboratory*; Bonaccorso, A., Calvari, S., Coltelli, M., Del Negro, C., Falsaperla, S., Eds.; AGU Geophysical Monograph Series; American Geophysical Union: Washington, DC, USA, 2004; Volume 143, pp. 1–27.
34. Azzaro, R.; Branca, S.; Gwinner, K.; Coltelli, M. The volcano-tectonic map of Etna volcano, 1:100,000 scale: Morphotectonic analysis from high-resolution DEM integrated with geologic, active faulting and seismotectonic data. *It. J. Geosci. (Boll. Soc. Geol. It.)* **2012**, *131*, 153–170.

35. Azzaro, R.; Castelli, V. Materiali per un Catalogo di Terremoti Etnei dal 1600 al 1831. *Quaderni di Geofisica*. 2015. Available online: <http://istituto.ingv.it/images/collane-editoriali/quaderni-di-geofisica/quaderni-di-geofisica-2015/quaderno123.pdf> (accessed on 23 December 2022).
36. Alparone, S.; Barberi, G.; Giampiccolo, E.; Maiolino, V.; Mostaccio, A.; Musumeci, C.; Scaltrito, A.; Scarfi, L.; Tuvè, T.; Ursino, A. Seismological constraints on the 2018 Mt. Etna (Italy) flank eruption and implications for the flank dynamics of the volcano. *Terra Nova* **2020**, *32*, 334–344. [[CrossRef](#)]
37. Borzi, A.M.; Giuffrida, M.; Zuccarello, F.; Palano, M.; Viccaro, M. The Christmas 2018 Eruption at Mount Etna: Enlightening how the volcano factory works through a multiparametric inspection. *Geochem. Geophys. Geosyst.* **2020**, *21*, e2020GC009226. [[CrossRef](#)]
38. Giampiccolo, E.; Cocina, O.; De Gori, P.; Chiarabba, C. Dyke intrusion and stress-induced collapse of volcano flanks: The example of the 2018 event at Mt. Etna (Sicily, Italy). *Sci. Rep.* **2020**, *10*, 6373. [[CrossRef](#)] [[PubMed](#)]
39. Civico, R.; Pucci, S.; Nappi, R.; Azzaro, R.; Villani, F.; Pantosti, D.; Cinti, F.R.; Pizzimenti, L.; Branca, S.; Brunori, C.A. Surface ruptures following the 26 December 2018, Mw 4.9, Mt. Etna earthquake, Sicily (Italy) EMERGEIO Working Group (Etna 2018). *J. Maps* **2019**, *15*, 831–837. [[CrossRef](#)]
40. Bruno, V.; Aloisi, M.; Gambino, S.; Mattia, M.; Ferlito, C.; Rossi, M. The Most Intense Deflation of the Last Two Decades at Mt. Etna: The 2019–2021 Evolution of Ground Deformation and Modeled Pressure Sources. *Geophys. Res. Lett.* **2022**, *49*, e2021GL095195. [[CrossRef](#)]
41. Lundgren, P.; Rosen, P.A. Source model for the 2001 flank eruption of Mt. Etna volcano. *Geophys. Res. Lett.* **2003**, *30*, 1388. [[CrossRef](#)]
42. Puglisi, G.; Bonforte, A.; Ferretti, A.; Guglielmino, F.; Palano, M.; Prati, C. Dynamics of Mount Etna before, during, and after the July–August 2001 eruption inferred from GPS and differential synthetic aperture radar interferometry data. *J. Geophys. Res.* **2008**, *113*, B06405.
43. Bonforte, A.; Guglielmino, F. Very shallow dyke intrusion and potential slope failure imaged by ground deformation: The 28 December 2014 eruption on Mount Etna. *Geophys. Res. Lett.* **2015**, *42*, 2727–2733. [[CrossRef](#)]
44. Bonforte, A.; Guglielmino, F.; Puglisi, G. Large dyke intrusion and small eruption: The December 24, 2018 Mt. Etna eruption imaged by Sentinel-1 data. *Terra Nova* **2019**, *31*, 405–412. [[CrossRef](#)]
45. De Novellis, V.; Atzori, S.; De Luca, C.; Manzo, M.; Valerio, E.; Bonano, M.; Cardaci, C.; Castaldo, R.; Di Bucci, D.; Manunta, M.; et al. DInSAR analysis and analytical modelling of Mt. Etna displacements: The December 2018 volcano-tectonic crisis. *Geophys. Res. Lett.* **2019**, *46*, 5817–5827. [[CrossRef](#)]
46. Palano, M.; Puglisi, G.; Gresta, S. Ground deformation patterns at Mt. Etna from 1993 to 2000 from joint use of InSAR and GPS techniques. *J. Volcanol. Geotherm. Res.* **2008**, *169*, 99–120. [[CrossRef](#)]
47. Cannata, A.; Di Grazia, G.; Giuffrida, M.; Gresta, S.; Palano, M.; Sciotto, M.; Viccaro, M. Space-Time evolution of magma storage and transfer at Mt. Etna volcano (Italy): The 2015–2016 re-awakening of voragine crater. *Geochem. Geophys. Geosyst.* **2018**, *19*, 471–495.
48. Azzaro, R.; Mattia, M.; Puglisi, G. Fault creep and kinematics of the eastern segment of the Pernicana Fault (Mt. Etna, Italy) derived from geodetic observations and their tectonic significance. *Tectonophysics* **2001**, *333*, 401–415. [[CrossRef](#)]
49. Froger, J.L.; Merle, O.; Briole, P. Active spreading and regional extension at Mount Etna imaged by SAR interferometry. *Earth Planet. Sci. Lett.* **2001**, *187*, 245–258. [[CrossRef](#)]
50. Lundgren, P.; Casu, F.; Manzo, M.; Pepe, A.; Berardino, P.; Sansosti, E.; Lanari, R. Gravity and magma induced spreading of Mount Etna volcano revealed by satellite radar interferometry. *Geophys. Res. Lett.* **2004**, *31*, L04602. [[CrossRef](#)]
51. Lundgren, P.; Berardino, P.; Coltelli, M.; Fornaro, G.; Lanari, R.; Puglisi, G.; Sansosti, E.; Tesauro, M. Coupled magma chamber inflation and sector collapse slip observed with synthetic aperture radar interferometry on Mt. Etna volcano. *J. Geophys. Res.* **2003**, *108*, 2247. [[CrossRef](#)]
52. Ferretti, A.; Prati, C.; Rocca, F. Permanent scatterers in SAR interferometry. *IEEE. T. Geosci. Remote* **2001**, *39*, 8–20. [[CrossRef](#)]
53. Berardino, P.; Fornaro, G.; Lanari, R.; Sansosti, E. A new algorithm for surface deformation monitoring based on small baseline differential SAR interferograms. *IEEE. T. Geosci. Remote* **2002**, *40*, 2375–2383. [[CrossRef](#)]
54. Neri, M.; Casu, F.; Acocella, V.; Solaro, G.; Pepe, S.; Berardino, P.; Sansosti, E.; Caltabiano, T.; Lundgren, P.; Lanari, R. Deformation and eruptions at Mt. Etna (Italy): A lesson from 15 years of observations. *Geophys. Res. Lett.* **2009**, *36*, L02309. [[CrossRef](#)]
55. Acocella, V.; Behncke, B.; Neri, M.; D’Amico, S. Link between major flank slip and 2002–2003 eruption at Mt. Etna (Italy). *Geophys. Res. Lett.* **2003**, *30*, 2286. [[CrossRef](#)]
56. Burton, M.R.; Neri, M.; Andronico, D.; Branca, S.; Caltabiano, T.; Calvari, S.; Corsaro, R.A.; Del Carlo, P.; Lanzafame, G.; Lodato, L.; et al. Etna 2004–2005: An archetype for geodynamically-controlled effusive eruptions. *Geophys. Res. Lett.* **2005**, *32*, L09303. [[CrossRef](#)]
57. Neri, M.; Acocella, V.; Behncke, B.; Maiolino, V.; Ursino, A.; Velardita, R. Contrasting triggering mechanisms of the 2001 and 2002–2003 eruptions of Mount Etna (Italy). *J. Volcanol. Geotherm. Res.* **2005**, *144*, 235–255. [[CrossRef](#)]
58. Bonaccorso, A.; Bonforte, A.; Guglielmino, F.; Palano, M.; Puglisi, G. Composite ground deformation pattern forerunning the 2004–2005 Mount Etna eruption. *J. Geophys. Res.* **2006**, *111*, B12207. [[CrossRef](#)]
59. Bonforte, A.; Gambino, S.; Guglielmino, F.; Obrizzo, F.; Palano, M.; Puglisi, G. Ground deformation modeling of flank dynamics prior to the 2002 eruption of Mt. Etna. *Bull. Volcanol.* **2007**, *69*, 757–768. [[CrossRef](#)]

60. Bonforte, A.; Bonaccorso, A.; Guglielmino, F.; Palano, M.; Puglisi, G. Feeding system and magma storage beneath Mt. Etna as revealed by recent inflation/deflation cycles. *J. Geophys. Res.* **2008**, *113*, B05406. [[CrossRef](#)]
61. Bonforte, A.; Gambino, S.; Neri, M. Intrusion of eccentric dikes: The case of the 2001 eruption and its role in the dynamics of Mt. Etna volcano. *Tectonophysics* **2009**, *471*, 78–86. [[CrossRef](#)]
62. Acocella, V.; Neri, M.; Norini, G. An overview of experimental models to understand a complex volcanic instability: Application to Mount Etna, Italy. *J. Volcanol. Geother. Res.* **2013**, *251*, 98–111. [[CrossRef](#)]
63. Palano, M.; Sparacino, F.; Gambino, P.; D'Agostino, N.; Calcaterra, S. Slow slip events and flank instability at Mt. Etna volcano (Italy). *Tectonophysics* **2022**, *836*, 229414. [[CrossRef](#)]
64. Palano, M. Episodic slow slip events and seaward flank motion at Mt. Etna volcano (Italy). *J. Volcanol. Geotherm. Res.* **2016**, *324*, 8–14. [[CrossRef](#)]
65. Azzaro, R.; Ferreli, L.; Michetti, A.M.; Serva, L.; Vittori, E. Environmental Hazard of Capable Faults: The Case of the Pernicana Fault (Mt. Etna, Sicily). *Nat. Hazard.* **1998**, *17*, 147–162. [[CrossRef](#)]
66. Urlaub, M.; Petersen, F.; Gross, F.; Bonforte, A.; Puglisi, G.; Guglielmino, F.; Krastel, S.; Lange, D.; Kopp, H. Gravitational collapse of Mount Etna's southeastern flank. *Sci. Adv.* **2018**, *4*, eaat9700. [[CrossRef](#)]
67. Goldstein, R.M.; Werner, C.L. Radar interferogram filtering for geophysical applications. *Geophys. Res. Lett.* **1998**, *25*, 4035–4038. [[CrossRef](#)]
68. Fialko, Y.; Simons, M.; Agnew, D. The complete (3-D) surface displacement field in the epicentral area of the 1999 MW7.1 Hector Mine Earthquake, California, from space geodetic observations. *Geophys. Res. Lett.* **2001**, *28*, 3063–3066. [[CrossRef](#)]
69. Just, D.; Bamler, R. Phase statistics of interferograms with applications to synthetic aperture radar. *Appl. Opt.* **1994**, *33*, 4361–4368. [[CrossRef](#)] [[PubMed](#)]
70. Herring, T.A.; King, R.W.; Floyd, M.A.; McClusky, S.C. *Introduction to GAMIT/GLOBK, Release 10.7*; Massachusetts Institute of Technology: Cambridge, UK, 2018. Available online: www-gpsg.mit.edu (accessed on 23 December 2022).
71. Saastamoinen, J. Atmospheric correction for the troposphere and stratosphere in radio ranging satellites. In *The Use of Artificial Satellites for Geodesy*; Henriksen, S.W., Mancini, A., Chovitz, B.H., Eds.; AGU Geophysical Monograph Series; American Geophysical Union: Washington, DC, USA, 1972; Volume 15, pp. 247–251.
72. Böhm, J.; Niell, A.; Tregoning, P.; Schuh, H. Global Mapping Function (GMF): A new empirical mapping function based on numerical weather model data. *Geophys. Res. Lett.* **2006**, *33*, L07304. [[CrossRef](#)]
73. Viccaro, M.; Zuccarello, F.; Cannata, A.; Palano, M.; Gresta, S. How a complex basaltic volcanic system works: Constraints from integrating seismic, geodetic, and petrological data at Mount Etna volcano during the July–August 2014 eruption. *J. Geophys. Res.* **2016**, *121*, 5659–5678. [[CrossRef](#)]
74. Chiarabba, C.; Amato, A.; Boschi, E.; Barberi, F. Recent seismicity and tomographic modeling of the Mount Etna plumbing system. *J. Geophys. Res.* **2000**, *105*, 10923–10938. [[CrossRef](#)]

Disclaimer/Publisher's Note: The statements, opinions and data contained in all publications are solely those of the individual author(s) and contributor(s) and not of MDPI and/or the editor(s). MDPI and/or the editor(s) disclaim responsibility for any injury to people or property resulting from any ideas, methods, instructions or products referred to in the content.